Broadband Field Localization, Density of States, and Nonlinearity Enhancement in Nonreciprocal and Topological Hotspots

Sander A. Mann,[1] Ahmed Mekawy,[1,2] and Andrea Alù[1,2,3,*]

[1] *Photonics Initiative, Advanced Science Research Center, City University of New York, New York 10031, USA*
[2] *Department of Electrical Engineering, City College of The City University of New York, New York 10031, USA*
[3] *Physics Program, Graduate Center, City University of New York, New York 10016, USA*

Enhancing light-matter interactions is necessary in a wide range of applications, such as sensing, nanophotonics, nonlinear and quantum optics. Nanoscale interactions are typically enhanced through localized resonances, resulting in a stringent trade-off between bandwidth, footprint, and overall enhancement factor. Here, we discuss how nonreciprocal electromagnetic hotspots, arising at the truncation of nonreciprocal and topological interfaces, can decouple these quantities, supporting extremely large and broadband field enhancements, leading to efficient nonlinear phenomena at the nanoscale and extreme broadband enhancement of local density of states. We discuss the impact of material nonlocality and surface roughness on these effects, providing closed-form expressions for the field enhancement in the presence of nonlocality and material loss, and demonstrating that many of these effects can be observed in several realistic scenarios. Finally, we outline how topological photonics can play a role in establishing these nonreciprocal hotspots. Our findings open opportunities to implement broadband nanophotonic platforms and metamaterials that exploit topological concepts to enable exotic light-matter interactions.

I. INTRODUCTION

Light interacts weakly with common materials, implying that meaningful light-matter interactions can typically be achieved only over large footprints. For nonlinear phenomena, large volumes of interactions require careful phase-matching considerations to make sure that contributions from different regions interfere constructively. By localizing and confining electromagnetic fields at the nanoscale through resonances, linear and nonlinear light-matter interactions can be dramatically enhanced. Plasmonics, in particular, has been proposed as a powerful platform to enable extreme light confinement, accompanied by dramatic enhancements of the electromagnetic fields [1] enabling a plethora of applications, from sensing [2], to manipulating light emission [3], and the quantum yield of emitters [4], achieving strong coupling with single molecules [5], and enhancing light absorption and nonlinear phenomena.

Approaches to field enhancements usually rely on resonant effects, which are associated with a sharp trade-off with the bandwidth of operation, drastically hindering the overall impact of these efforts for many applications. Recent approaches to overcome these challenges

have involved the use of adiabatic transitions into ultra-confined plasmonic slow light modes and singular plasmonic geometries. These solutions enhance the fields over broader bandwidths, but typically involve other trade-offs, including large footprints and sensitivity to geometrical features and disorder. In this paper, we discuss a different mechanism to achieve field localization and enhanced light-matter interactions, which relies on nonreciprocal, unidirectional waveguides supporting a single forward mode of propagation. There has been significant recent interest in unidirectional waveguides, as they enable, e.g., propagation robust against arbitrarily strong disorder [6–10] and broadband matching in small footprints [11–13]. These unidirectional waveguides can arise at the interface between materials with different band-structure topologies (characterized by their Chern number) [7,8,14], analogous to the quantum Hall effect in solid-state physics [15].

Some unidirectional waveguide geometries can be terminated without creating a radiative outgoing channel, due to the absence of a backward mode in the waveguide or surface modes along the termination [16–19]. Interestingly, the absence of a backward channel in these waveguides implies the necessary emergence of a nonreciprocal hotspot at the termination [16,18–22], at which the electromagnetic fields are largely enhanced over the entire unidirectional bandwidth. Here, we discuss the phenomena

*aalu@gc.cuny.edu

arising at these unusual field singularities in detail and show how they can provide exciting opportunities for enhanced, broadband nonlinear interactions and local density of state (LDOS) enhancements that overcome the mentioned trade-offs with bandwidth, footprint, and sensitivity to disorder. We provide an accurate analytical approximation for the enhancement that enables straightforward comparison between different material systems. Subsequently, we discuss the resilience of these field enhancements to nonlocality and surface roughness. Finally, we discuss the role that topological protection can play in supporting these phenomena.

II. PLASMONIC FIELD ENHANCEMENTS

Large field enhancements in plasmonic systems rely on localized resonant oscillations of electrons at a metallic interface [4,5]. While these resonances are typically associated with a rather low quality factor due to unavoidable material loss, the overall light-matter interactions are dramatically boosted by their extremely small mode volume. For example, the resonant enhancement of the decay rate of a quantum emitter is described by the Purcell factor, $F = 3Q\lambda^3/(4\pi^2 V)$ [23], where Q is the resonance quality factor, λ is the wavelength in the host medium, and V is the mode volume [24,25]. A lower quality factor reduces the enhancement factor, but for plasmonic systems this reduction can be more than offset by their very small mode volume compared to dielectric resonators [26], e.g., in nanopatch antennas [4].

Figure 1(a) shows the schematic of a plasmonic bowtie antenna, which supports a bonding mode between the two metal arms yielding extreme field localization [27, 28]. The high fields at this electromagnetic hotspot have been used for nonlinear harmonic generation [29] and enhanced single-emitter fluorescence [3,30]. Field enhancements of over 3 orders of magnitude can be realistically achieved [27,28], but the bandwidth over which this enhancement occurs is naturally limited by the resonance linewidth, and a trade-off between these two quantities is expected.

Simultaneously enhancing bandwidth *and* field enhancement is challenging, but also highly desirable, as it would enable efficient and compact, yet broadband, nanophotonic devices, nonlinear nanostructures, and sensors. A promising approach to achieve broadband field enhancement is through adiabatic plasmonic nanofocusing [31–35]: if the width of a plasmonic metal-insulator-metal (*M-I-M*) waveguide is slowly tapered down [36,37], as shown in Fig. 1(b), the supported mode slows down and the field intensity correspondingly increases. Provided that the taper is sufficiently long and smooth, no reflections occur all the way to the apex, where the group velocity vanishes independent of frequency across the entire bandwidth in
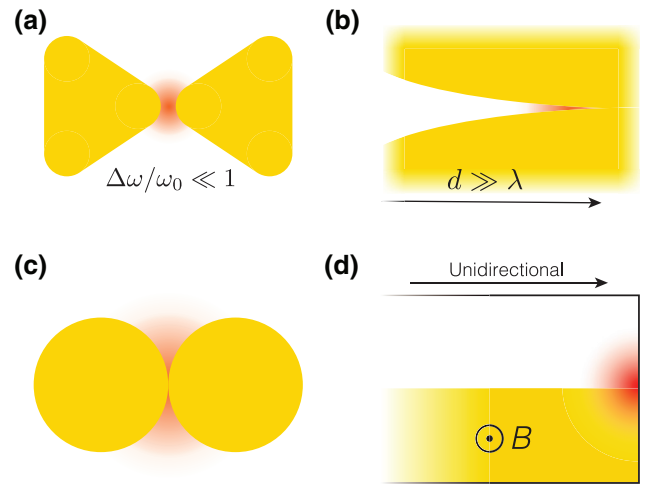

FIG. 1. (a) A bowtie plasmonic nanoantenna supports an electromagnetic hotspot (red). As a resonant phenomenon, the fractional bandwidth of field enhancement is inherently small, and inversely proportional to the field enhancement. (b) A plasmonic adiabatic transition into a hotspot supports a much larger bandwidth, at the expenses of a large footprint to achieve adiabaticity. (c) Touching plasmonic cylinders combine a small footprint with an adiabatic transition to a hotspot, but at the cost of enhanced sensitivity to disorder. (d) The hotspot at the termination of a unidirectional waveguide totally decouples bandwidth and field enhancement.

which the plasmonic mode is supported. As a result, broadband field enhancements can be achieved. Here, however, footprint is traded with bandwidth: in order to ensure that the incident waveguide mode is not reflected, the transition needs to be gradual, and the larger the bandwidth, the longer the adiabatic taper that is required.

The merits of the two approaches in Figs. 1(a) and 1(b) may be combined considering the geometric singularities arising at the sharp plasmonic tips of cones or wedges [38–40]. Quasistatic diverging fields arise at these singular points for a wide range of angles and material parameters [39], with inherently broadband properties. Structures containing such singularities can also be designed through transformation optics [41,42], mapping, for instance, a parallel *M-I-M* waveguide into touching cylinders with much reduced footprint [41,43,44] [Fig. 1(c)]. Similar to the adiabatically tapered scenario, as plasmons travel towards the apex of the touching cylinders, they become slower and increasingly confined. Large field strengths hence emerge over a wide bandwidth, but also in a compact footprint. These benefits, however, are traded with enhanced sensitivity to disorder, as tiny imperfections on the surface of the cylinders near the apex drastically change the response and introduce large reflections and losses.

Nonreciprocal and topological singularities arising in terminated unidirectional waveguides, as schematically

shown in Fig. 1(d), offer the opportunity to overcome these trade-offs. These geometries provide giant field enhancement over the entire bandwidth for which the waveguide is unidirectional, in a compact footprint that avoids tapering requirements and with inherently strong robustness to disorder and imperfections associated to their topological features. These field singularities were studied in the 1960s [16,21] in the context of a perceived thermodynamic paradox arising in unidirectional waveguides that carry power only one way. Because no backward flow of power is allowed in these waveguides, it was shown that they must support electromagnetic hotspots at their termination in which the incoming energy gets fully dissipated over the entire unidirectional bandwidth, independent of the actual level of material loss. The recent interest in integrated nonreciprocal and topological devices has caused a renewed interest in these nonreciprocal hotspots due to their large field strengths, wide bandwidths, and small footprint [10,18,19,21,22,45]. These hotspots are somewhat analogous to the adiabatically tapered waveguide in Fig. 1(b), with the exception that there is no need for a carefully tapered adiabatic transition, since the lack of a backward mode ensures the absence of reflection and impedance matching [21].

In this paper, we discuss the field enhancement that can occur in these nonreciprocal hotspots in detail, placing them into context with the field enhancements obtained with known reciprocal plasmonic structures. We present two relevant applications of these hotspots, broadband enhancement of nonlinear effects and of local density of states. We then discuss the implications that nonlocality and absorption losses enforce in these systems, deriving an accurate analytical expression for the expected field enhancement. We show that, even in the case of realistic materials, these nonreciprocal waveguides provide major benefits over their reciprocal counterparts when it comes to backscattering losses from surface roughness, and finally, we discuss the potential impact and limitations of nonreciprocal topological systems for such field enhancements.

III. UNIDIRECTIONAL PROPAGATION AT NONRECIPROCAL INTERFACES

For completeness we start by reviewing the fundamentals of unidirectional plasmonic waveguides, and the role that nonlocality and material loss impose on their response. Consider the propagation of a surface plasmon polariton at the interface between a dielectric and a magnetically biased metal with gyrotropic permittivity [46]

$$\varepsilon(\omega) = \varepsilon_0 \begin{pmatrix} \varepsilon_1 & i\varepsilon_2 & 0 \\ -i\varepsilon_2 & \varepsilon_1 & 0 \\ 0 & 0 & \varepsilon_3 \end{pmatrix}, \quad (1)$$

where ε_0 is the vacuum permittivity, and

$$\varepsilon_1 = \varepsilon_\infty - \frac{(\omega - i\gamma)\omega_p^2}{\omega[(\omega - i\gamma)^2 - \omega_c^2]},$$

$$\varepsilon_2 = \frac{\omega_c \omega_p^2}{\omega[(\omega - i\gamma)^2 - \omega_c^2]}, \quad (2)$$

$$\varepsilon_3 = \varepsilon_\infty - \frac{\omega_p^2}{\omega(\omega - i\gamma)}.$$

Here ω_p is the plasma frequency, γ is the damping rate, ε_∞ is the relative permittivity due to bound electrons, and $\omega_c = eB/m_e$ is the cyclotron frequency, with e the elementary charge, $B = \mathbf{B} \cdot \hat{z}$ the magnetic induction, and m_e the effective electron mass. A similar permittivity tensor can be found in axionic materials, which have recently garnered attention and may provide similar opportunities [47,48].

The permittivity tensor in Eq. (1) is asymmetric, and therefore nonreciprocal. A strong nonreciprocal response is achieved maximizing the skew-symmetric part of Eq. (1) with respect to the diagonal elements. Practically, this can be achieved by selecting a material with a low effective electron mass, so that ω_c is large even for limited magnetic bias strengths. For this reason, InSb has been the material of choice in many recent theoretical studies of unidirectional plasmon propagation [10,19,21,49]: its effective mass at room temperature is only $m_e \approx 0.012m_0$, where m_0 is the electron mass, considerably lower than most metals or semiconductors, enabling a strong nonreciprocal response at low magnetic bias strengths. In the following, we focus on undoped InSb, with intrinsic carrier density $n_i = 1.8 \times 10^{16}$ cm^{-3}, resulting in plasma frequency $\omega_p = \sqrt{n_i e^2/\varepsilon_0 m_e} = 6.85 \times 10^{13}$ rad s^{-1} and damping rate $\gamma = e/(m_e \mu_e) \approx 0.027\omega_p$, where μ_e is the electron mobility [50].

In Fig. 2 we study the propagation of surface plasmon polaritons in the x direction at an interface of this material with silicon, with relative permittivity $\varepsilon_d = 11.68$, under a static magnetic field bias along z, consistent with recent theoretical papers [6,13,19,21,45]. A sketch of the waveguide is shown in Fig. 2(a), consisting of a metal-dielectric interface encapsulated by two perfect electric conductor (PEC) planes. A top PEC in close proximity to the metal-dielectric interface is necessary to make the waveguide truly unidirectional, by ensuring that higher-order modes are at cutoff, and that it is not possible to scatter into free space. The bottom PEC facilitates collection of second-harmonic generation, which is above the plasma frequency of the metal, as discussed in Sec. VI. Figure 2(b) shows the modal dispersion of the waveguide without (blue) and with (red) magnetic field bias, for $B = 0.31$ T. In the presence of a magnetic field bias
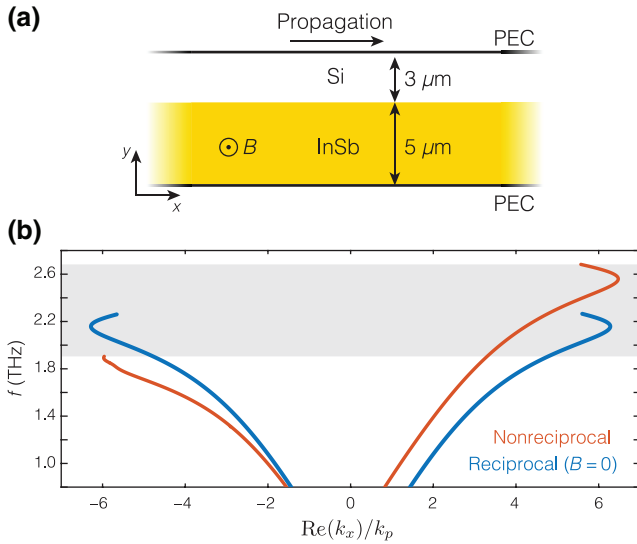
(a)

(b)

FIG. 2. (a) Schematic of the unidirectional plasmon polariton waveguide under consideration. (b) Dispersion of the waveguide without (blue) and with (orange) magnetic bias. In the biased scenario ($B = 0.31$ T), the waveguide has a unidirectional window, shown in gray. We show dispersion curves until $\mathrm{Im}(k_x) > \mathrm{Re}(k_x)$.

polarized in the negative z direction, the forward plasmon asymptote moves to higher frequencies, while the backward asymptote moves to lower frequencies [6,10,13, 18,19]. This opens a frequency window of unidirectional propagation, as highlighted in gray.

IV. NONRECIPROCAL HOTSPOTS

We terminate the nonreciprocal polaritonic waveguide with a PEC wall, producing an accumulation of electromagnetic energy at the nonreciprocal hotspot formed at the corner [18,19,21], as shown schematically in Fig. 3(a). Unless otherwise mentioned, results in the remainder of the paper are calculated with COMSOL Multiphysics (see Appendix). The electric field norm at 2.2 THz (in the middle of the unidirectional frequency window) is shown in Fig. 3(b), with a color scale limited to a field enhancement factor of 300 to enhance visibility of the hotspot. Here the enhancement is measured relative to the field strength of the incoming wave exciting the structure. The field enhancement becomes very large as we approach the corner: Fig. 3(c) shows the enhancement along the interface, reaching a peak of over 10^4. Near the termination, the field strength grows with an inverse power law ($|\mathbf{E}| \propto r^{-\nu}$, where ν is a constant larger than 1), characteristic of this class of quasistatic wedge modes [38,39]. The maximum enhancement is inversely proportional to the loss rate of the material, ensuring that Poynting's theorem is satisfied at the termination, and all incident power is

(a) Unidirectional waveguide   Hotspot **(b)**
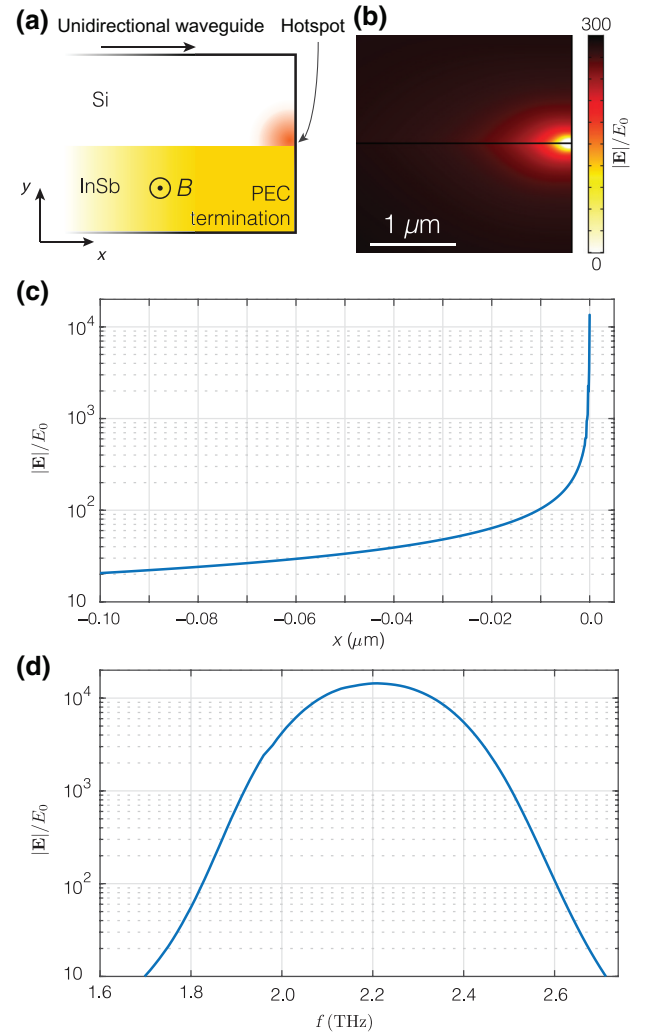

(c)

(d)

FIG. 3. (a) Sketch of the nonreciprocal hotspot geometry. (b) Magnitude of the electric field at 2.2 THz near the hotspot, where the color scale is capped at an enhancement factor of 300 to enhance visibility. (c) Magnitude of the electric field at the Si/InSb interface versus distance to the termination. (d) Field at the PEC/Si/InSb corner as a function of frequency over the unidirectional window.

absorbed [16]. The fields are significantly enhanced over the entire unidirectional bandwidth, as shown in Fig. 3(d).

This broadband, large enhancement does not follow the typical trade-offs of a conventional resonant system (reciprocal or nonreciprocal [21]), offering exceptional benefits for nanophotonic applications. We demonstrate this claim by comparing the field enhancement at the nonreciprocal hotspot to those obtained in the bowtie antenna and the touching cylinders configurations in Figs. 1(a) and 1(c). To be able to make a fair comparison, these geometries are also embedded in silicon and placed in a terminated parallel plate waveguide, akin to the nonreciprocal hotspot geometry. The arms of the bowtie antenna have a 1 μm
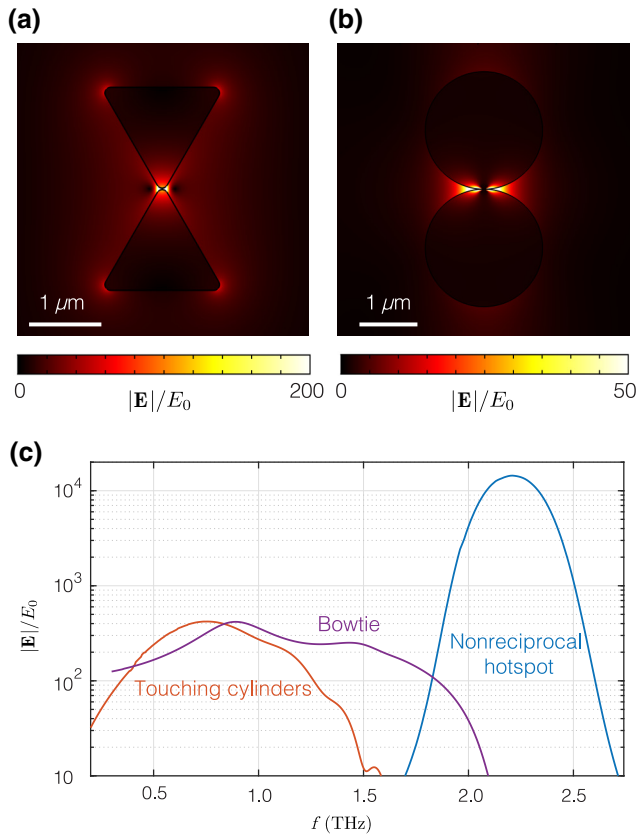
FIG. 4. Electric field intensity in (a) the bowtie antenna at 1.08 THz, and (b) the touching cylinders at 1.1 THz. In these electric colormaps the scale is clipped to enhance visibility of the hotspot. (c) Spectral comparison of the electric field enhancement between the bowtie antenna, touching cylinders and nonreciprocal hotspot in Fig. 3. In all subfigures, the electric field amplitude is normalized to the electric field amplitude E_0 in the input plane wave.

height, while the cylinders forming the touching cylinders have a 1 μm radius. The electric field distribution is shown for both geometries in Figs. 4(a) and 4(b), respectively, and may be compared with the nonreciprocal hotspot in Fig. 3(b). The field enhancement versus frequency for optimal location in each geometry is shown in Fig. 4(c). For the bowtie antenna, the field maximum is observed exactly at the center of the bowtie, and we find about five resonant peaks in the electric field amplitude, corresponding to different plasmonic resonances. The lowest-order resonance has the highest field enhancement, with a factor of 10^3, and the largest bandwidth over which the enhancement takes place. If we consider the unitless figure of merit $|\mathbf{E}|\Delta\omega/(E_0\omega_0)$, which is the product of the peak field enhancement multiplied by the fractional bandwidth over which the amplitude is above $1/\sqrt{(2)}$ of the peak amplitude, we find a bandwidth-enhancement product of 169.

The touching cylinders offer a comparable field enhancement to the bowtie, but over a larger bandwidth, consistent with recent papers [43,44] and as shown in Fig. 4(c) (red curve). While the structure is small in footprint, it makes use of the extremely large plasmon wave numbers near the apex to support a very large number of resonances, which form a continuous band of field enhancement for sufficiently large material loss. The peak field enhancement is over 420 with a fractional bandwidth of 0.53, resulting in a bandwidth-enhancement product of 223—larger than the bowtie antenna. For lower loss rates, the bandwidth-enhancement product can be significantly enhanced: both bandwidth and field enhancement increase, while for the bowtie antenna the enhancement factor increases, but the bandwidth reduces (as the enhancement stems from a single resonance).

We now turn our attention to the bandwidth-enhancement factor of the nonreciprocal hotspot, shown again in Fig. 4(c) in blue. While the fractional bandwidth of 0.14 is smaller than in both previous geometries, the peak field enhancement of 1.4×10^4 is almost 2 orders of magnitude larger. This results in a figure of merit of 2.1×10^3, significantly exceeding the bowtie and touching cylinders antennas. We stress also that the bandwidth of operation here is simply controlled by the frequency range over which unidirectional propagation is supported by the waveguide, and a larger magnetic bias, or different material dispersion, directly translates in a larger bandwidth, independent of the termination geometry [10]. Such decoupling between bandwidth and field concentration, and the enhanced bandwidth-enhancement product combined with large field confinement at the nanoscale, are ideal features in a number of nanophotonic applications, such as emission control through the local density of optical states and strong nonlinear phenomena without the need for phase matching. Very remarkable as well is the resilience of this response on the specific geometry of the termination, or of the possible presence of imperfections and disorder, which would dramatically alter the resonant response of the touching cylinders and bowtie antenna. In the following sections, we discuss the implication of these findings for practical nanophotonic applications, as well as the implications of nonlocality and disorder.

V. BROADBAND LDOS ENHANCEMENT IN NONRECIPROCAL HOTSPOTS

The amount of power radiated by an electromagnetic emitter for a fixed current depends on its environment. In the field of antennas, for instance, the effect of the distance to a ground plane on the radiation resistance and the overall radiated power has been discussed by van der Pol over a century ago [51]. In photonics, Purcell

considered spontaneous emission from localized quantum sources, showing that coupling to a resonant cavity may dramatically enhance their decay rate [23]. The effect of the environment on the spontaneous emission rate of fluorophores was later experimentally demonstrated by Drexhage, who showed that the emitter decay rate is affected by its distance to an interface, similar to the antenna and ground-plane problem [52]. More recently, there have been numerous demonstrations highlighting the role of the local environment for localized emitters in optics and other wave phenomena [4,53,54].

A relevant quantity to describe the modification of the decay rate is the local density of optical states [55]. The electric field at $\mathbf{r}_o$ due to a point source located at $\mathbf{r}_s$ is generally given by

$$\mathbf{E}(\mathbf{r}_o) = \omega^2 \mu_0 \overleftrightarrow{\mathbf{G}}(\mathbf{r}_o, \mathbf{r}_s) \cdot \mathbf{p}_s, \qquad (3)$$

where $\mathbf{p}_s$ is the point-source dipole moment, $\overleftrightarrow{\mathbf{G}}$ is the dyadic Green function, and μ_0 is the free-space permeability. Given the Green function, the LDOS can be calculated by evaluating it at the source position through $6\omega\{\mathbf{d}^\dagger \cdot \mathrm{Im}[\overleftrightarrow{\mathbf{G}}(\mathbf{r}_s, \mathbf{r}_s) \cdot \mathbf{d}]/(\pi c^2)\}$, where $\mathbf{d} = \mathbf{p}/|\mathbf{p}|$ is a unit vector in the direction of the dipole moment. Achieving a large LDOS is desirable, for example, in the pursuit of fast, bright, single-photon sources [26,56], which are considered a useful resource for quantum communications. Harvesting single photons at will with 100% efficiency requires a dramatic reduction of the emitter lifetime (usually on the order of nanoseconds) and emission into a single mode [57].

A nanophotonic structure with a large LDOS, directing radiation from an emitter into a certain direction, will also have large electric field strengths at the emitter location when excited *from* that direction. This is a consequence of the following identity for reciprocal, linear, time-invariant media:

$$\overleftrightarrow{\mathbf{G}}(\mathbf{r}_A, \mathbf{r}_B) = \overleftrightarrow{\mathbf{G}}^T(\mathbf{r}_B, \mathbf{r}_A), \qquad (4)$$

where A and B indicate two arbitrary locations. A corollary of Eq. (4) is the Lorentz reciprocity theorem (for single-point sources):

$$\mathbf{E}_A \cdot \mathbf{p}_B = \mathbf{E}_B \cdot \mathbf{p}_A. \qquad (5)$$

In other words, this equality implies that if a point source at point A induces a field at point B, then a point source at point B necessarily induces an equally strong field at A.

Intuitively, it is much more straightforward to estimate an antenna's performance as a decay rate enhancer from Lorentz reciprocity, than it is based on the Green function at the source location, $6\omega\{\mathbf{d}^\dagger \cdot \mathrm{Im}[\overleftrightarrow{\mathbf{G}}(\mathbf{r}_s, \mathbf{r}_s) \cdot \mathbf{d}]/(\pi c^2)\}$. However, it is well known that in nonreciprocal media,

Eqs. (4) and (5) do not hold. In fact, this is what makes nonreciprocity necessary for applications such as isolators. The role nonreciprocity may play in enhancing the LDOS, however, has not been investigated yet, and is also not immediately apparent because the intuitive argument based on Lorentz reciprocity cannot be applied.

Here, we show that nonreciprocity in fact can result in extremely large and broadband LDOS enhancements. This is most easily understood from more general forms of Eqs. (4) and (5), which can be derived [58,59] by using the time-reversal properties of the constitutive relations [60,61] and Casimir-Onsager reciprocity [62]:

$$\mathbf{G}(\mathbf{r}_A, \mathbf{r}_B, \mathbf{H}_0) = \mathbf{G}^T(\mathbf{r}_B, \mathbf{r}_A, -\mathbf{H}_0), \qquad (6)$$

$$\mathbf{E}_A(\mathbf{H}_0) \cdot \mathbf{p}_B = \mathbf{E}_B(-\mathbf{H}_0) \cdot \mathbf{p}_A. \qquad (7)$$

Equation (7) implies that the large, broadband field enhancement obtained in the nonreciprocal hotspot [Fig. 3(d)] when excited by a point source far away in the waveguide necessarily results in a large, broadband LDOS when the orientation of the static magnetic field is reversed. This is schematically shown in Figs. 5(a) and 5(b).
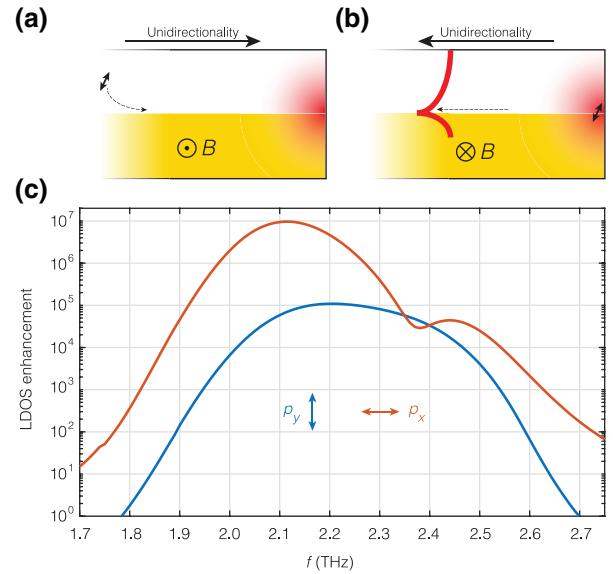

FIG. 5. (a) A localized emitter excites the unidirectional polariton mode, which accumulates energy in the nonreciprocal hotspot and it results in large, broadband field intensities. (b) As a consequence of Eq. (7), when the magnetic bias is reversed and the unidirectionality changes direction, an emitter at the location of the hotspot experiences a large, broadband LDOS enhancement. (c) LDOS enhancement for a source located at the hotspot, as in (b). The enhancement is calculated as the radiated power normalized to the radiated power by a source with the same orientation in an infinite waveguide unidirectional waveguide.

To confirm that the LDOS is indeed very large, we place a localized emitter in the hotspot at the termination and reversed the magnetic bias direction. The resulting radiative LDOS enhancements are shown in Fig. 5(c), where we normalize the radiated power to the power radiated by a source with the same orientation in an infinite unidirectional waveguide. As expected from Eq. (7), the enhancement is extremely large (reaching an enhancement factor of over 10^7) over the entire unidirectional bandwidth, similar to the field enhancement observed in Figs. 3 and 4. The enhancement is largest in the x polarization, as expected given the boundary conditions at the PEC termination that require that fields parallel to the interface vanish.

The broadband enhancement observed here provides interesting opportunities to enhance the decay rate of localized optical sources, even in scenarios in which they already decay fast by themselves, or to enhance the decay rate of multiple, spectrally separated single-photon sources. Furthermore, the emission happens into a single localized mode that is robust against disorder, enhancing collection efficiencies. Finally, the dramatic gradient of field enhancement at small distances [as observed in Fig. 3(c)] may provide an effective means to access higher-order, normally forbidden transitions [63] or to investigate ultrastrong coupling phenomena in unidirectional systems [64,65]. All these features make the nonreciprocal hotspot discussed here promising in the context of classical and quantum nanophotonic systems and applications.

VI. BROADBAND NONLINEAR OPTICS

Nonlinear optics is another field of optics that relies on high field intensities. Nonlinear susceptibilities are weak in naturally occurring materials, requiring large footprints to achieve, e.g., significant harmonic conversion efficiencies, with the added complication of phase-matching requirements. For this reason, there has been considerable interest in nanophotonic engineering of materials to enhance nonlinear phenomena to the point that sufficient nonlinear phenomena can arise in subwavelength volumes. The field confinement offered by plasmonic resonators has proven to be successful to enhance nonlinear effects [66,67], even though with limitations associated with enhanced material loss and the limited bandwidth over which large enhancement can be achieved.

In this context, it has recently been reported that non-reciprocal hotspots may lead to large enhancements for third-harmonic generation [68]. Here, we investigate the benefits of the hotspot for nonlinear optics looking at second-harmonic generation (SHG), and compare the performance to touching plasmonic cylinders. We assume a nonlinear susceptibility $\chi^{(2)}$ that sustains a current density

$$J_i^{(2\omega)} = 2i\omega\varepsilon_0 \chi_{ijk}^{(2)} E_j^{(\omega)} E_k^{(\omega)}. \tag{8}$$

We place a small (100 by 100 nm) nonlinear particle with $\chi_{ijk}^{(2)} = 20$ pV/m close to the hotspot in Fig. 3, representative of materials with strong nonlinear responses. For simplicity, we focus on polarization preserving nonlinear susceptibilities [$\chi_{xxx}^{(2)}$ and $\chi_{yyy}^{(2)}$], which can be found in materials such as $LiNbO_3$ and multiquantum wells.
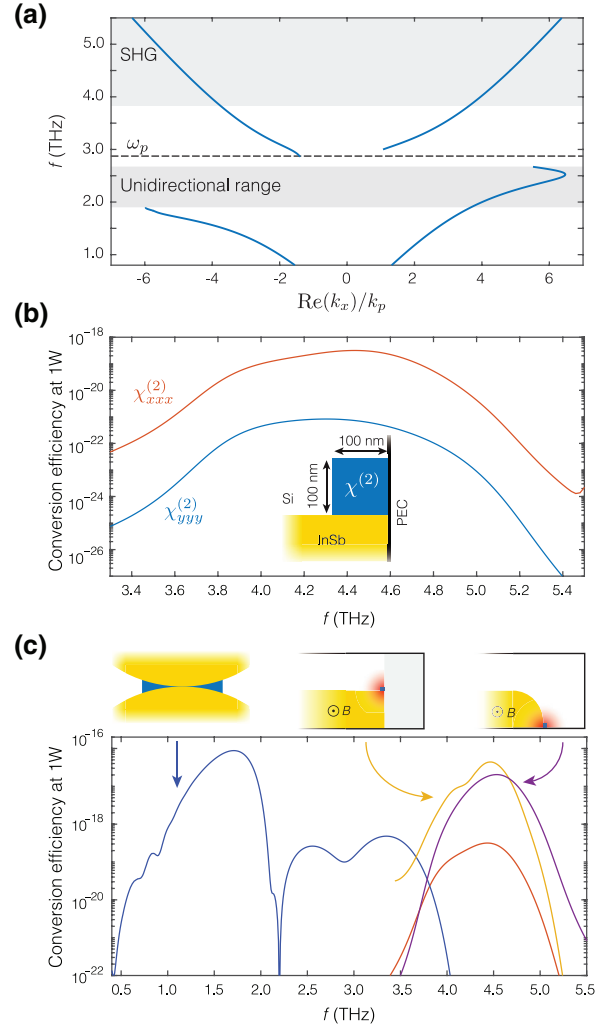

FIG. 6. (a) Dispersion of the nonreciprocal waveguide, showing the one-way polariton mode, as well as a second mode at the PEC/InSb interface at low frequencies and a high-frequency dielectric parallel plate mode above the plasma frequency, responsible for carrying second-harmonic radiation. (b) Second-harmonic conversion efficiency for the geometry shown in the inset. The conversion efficiency, calculated for 1-W input power, roughly follows the same spectral features as the fundamental field intensity. (c) Comparison between the touching cylinders (blue, geometry shown above) and the configuration in (b), shown in red. As the LDOS at the termination is low due to the boundary conditions, two improved nonreciprocal hotspot geometries are shown above the plots for more efficient SHG (yellow and purple curves).

Because the conversion efficiency is quadratic in the fundamental field strength, we design the conversion process so that the fundamental frequency lies within the unidirectional window supporting the nonreciprocal hotspot. At the second-harmonic frequency, the waveguide is bidirectional despite the magnetic bias, consistent with the dispersion diagram in Fig. 6(a), but the waveguide is still single mode due to its limited height of 8 μm. This enables feeding the nonreciprocal hotspot at the fundamental frequency through the one-way polariton mode, and at the same time efficiently collecting the second harmonic through the backward propagation of a single mode at double the frequency. In Fig. 6(a), both the unidirectional window as well as the window where we expect to collect efficient second-harmonic generation are shown.

For an input power of 1 W, we find the spectral conversion efficiencies shown in Fig. 6(b), where the position of the nonlinear inclusion is schematically shown in the inset. In the unidirectional frequency range, the conversion efficiency for $\chi^{(2)}_{xxx}$ is about 2 orders of magnitude larger, a consequence of the boundary condition at the PEC termination: the electric fields parallel to the surface must vanish, and the radiated power for a source parallel to a ground plane therefore also vanishes. However, at 2ω the response of InSb is dielectric ($2\omega > \omega_p$) and hence the electric field in the corresponding guided mode is largely y polarized, making the radiation efficiency close to the PEC termination poor. Additionally, for both orientations the overall conversion efficiency is quite low due to the small size of the nonlinear particle and the low input power.

The role of the LDOS at 2ω becomes more apparent when we compare the obtained conversion efficiency to the touching cylinders scenario, shown in blue in Fig. 6(c) (the position of the 10^4 nm^2 nonlinear inclusion is shown in the schematic). Even though the field strength at the fundamental frequency is orders of magnitude lower than at the nonreciprocal hotspot, as shown in Fig. 4(d), the overall conversion efficiency is larger due to the enhanced LDOS at the second harmonic, as well as more confined fields due to the small opening angle near the apex. The dips in conversion efficiency are due to interference with the reflector.

To boost the conversion efficiency of the nonreciprocal hotspot, we pursue two approaches. The first is to adjust the location of the PEC/Si/InSb junction: given that the field at the second harmonic is largely y polarized, moving the hotspot to the bottom PEC, as shown in the inset in Fig. 6(b), significantly enhances the LDOS while preserving the hotspot field strength. The result is shown in Fig. 6(c) in yellow, where the $\chi^{(2)}_{xxx}$ conversion efficiency of Fig. 6(b) is shown again for reference. The second approach is to not terminate the waveguide into a perfect electric conductor, but instead choose a metal with plasma frequency between the fundamental and second

harmonic. This results in a metallic response at the fundamental frequency, providing the termination, while at the second harmonic the response is dielectric, resulting in a different boundary condition and a significantly enhanced LDOS. The conversion efficiency for a termination comprising a 15-μm segment of Drude metal with $\varepsilon_\infty = 3.2$ and $\omega_p = 6\pi \times 10^{12}$ rad/s, is shown in Fig. 6(c) in black, again showing promising features for broadband nonlinear enhancement. Once again, we stress the inherent resilience of these phenomena to variations in the geometrical parameters or disorder, drastically different from conventional plasmonic resonators.

VII. NONLOCAL PHENOMENA

Extreme plasmonic effects are typically limited by material loss. However, in the limit of negligible material loss, nonlocal effects (also referred to as spatial dispersion) enter into play to fundamentally limit the available field localization [69]. Nonlocal phenomena, which arise when the polarization field depends not only on the electric field at the same location, but also on the electric field in its proximity, become significant in extreme field localization phenomena, because the corresponding field variations arise at very small length scales. In Fourier space, the nonlocal electromagnetic response expresses itself as a wave-vector-dependent permittivity. These issues become relevant also in the unidirectional polariton mode discussed in the previous sections: recently, it was demonstrated that the presence of nonlocality introduces a high-k backward mode within the unidirectional window in Fig. 2 [70], yielding a radiative pathway for incident power to leave the termination. This makes sense: it is clear that for sufficiently large k any material response must vanish, as the polariton wavelength becomes comparable or even smaller than the atomic scale, hence at some point nonlocality must kick in and get rid of the unidirectional response. In the following, we explore the implications of this finding in the context of nonreciprocal broadband field enhancements and demonstrate that realistic nonlocal responses preserve the main conclusions drawn in the previous sections.

The most common approach to describe material nonlocality is provided by the hydrodynamic model, introduced by Bloch in 1933 [71,72]. Using this model, a number of high-symmetry scenarios can be solved analytically [50], and alternatively hydrodynamic nonlocality can be efficiently incorporated in numerical simulations. The hydrodynamic model is implemented by considering an additional differential equation for the current density $\mathbf{J}(\mathbf{r}) = en(\mathbf{r})\mathbf{v}(\mathbf{r})$, where $n(\mathbf{r})$ and $\mathbf{v}(\mathbf{r})$ are the spatially dependent electron density and velocity [70,72]:

$$\beta^2 \nabla(\nabla \cdot \mathbf{J}) + \omega(\omega - i\gamma)\mathbf{J} = i\omega \left(\omega_p^2 \varepsilon_0 \varepsilon_\infty \mathbf{E} - \frac{e}{m_e}\mathbf{J} \times \mathbf{B} \right).$$

$$(9)$$

Here, β is related to the Fermi velocity v_F by $\beta^2 = 3v_F^2/5$ (considering the Thomas-Fermi model for the electron gas). It is the nonlocal parameter determining the strength of the pressure term, in analogy with hydrodynamics, which works to homogenize irregularities in $n(\mathbf{r})$, smearing the material response on a characteristic length scale $\xi \sim \beta/\omega$ [73]. In addition to convective currents following from the pressure term, it is also possible to incorporate electron diffusion [72], but we neglect these effects here. To incorporate the nonlocal response, Eq. (9) is coupled with Maxwell's equations through

$$\nabla \times \nabla \times \mathbf{E} = \frac{\omega^2}{c^2}\varepsilon_\infty \mathbf{E} + i\omega\mu_0 \mathbf{J} \qquad (10)$$

(where μ_0 is the vacuum permeability). The resulting set of equations can be solved numerically, as we do here, or analytically in high-symmetry scenarios.

For intrinsic semiconductors, β is determined by material properties according to $\beta^2 = 3k_B T/m_e$, yielding $\beta_0 = 1.07 \times 10^6$ m/s for InSb at room temperature [50]. This value is large compared to other metals and semiconductors, because the effective electron mass is low—exactly the reason why the unidirectional window is also large for moderate magnetic bias, as previously mentioned. To study the effect of nonlocality on the nonreciprocal hotspot, we consider the different scenarios $\beta = 0$, $\beta = 0.25\beta_{\text{InSb}}$, $\beta = \beta_{\text{InSb}}$ in Fig. 7(a). The color plots show the electric field norm near the termination at 2.15 THz, where the local scenario $\beta = 0$ is consistent with the previous sections. The confinement at the termination decreases with increasing nonlocality, as expected, with the beating pattern indicating interference between the forward mode and a more confined backward mode, absent in the local scenario (to enhance the visibility of the beating, we reduce the loss rate for simulations in this figure by a factor of 4). The point of highest intensity also moves further away from the termination, and its location is determined by constructive interference between forward and backward modes. The backwards mode is highly confined, due to its large momentum, resulting in large field strengths close to the interface. As such, the mechanism behind the large field strengths is similar to the case of narrow plasmonic slot waveguides, where large momenta and strong confinement lead to large fields and slow group velocities [74]. Here we still observe the advantage of resilience to disorder and automatic impedance matching at the termination, given that the strongly confined backward mode decays very fast. To gauge more clearly how the field enhancement depends on the material nonlocality, in Fig. 7(b) we show the enhancement along the interface close to the termination as a function of β. The nonreciprocal hotspot is recovered for small β, where the backwards wave number
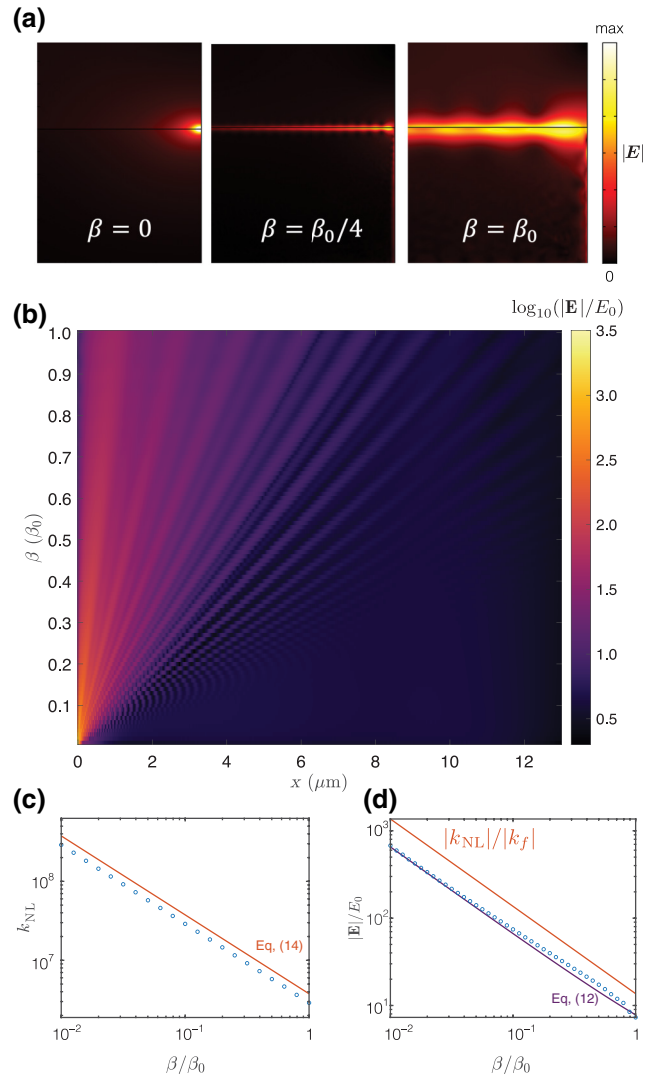

FIG. 7. (a) Electric field magnitude near the termination for three nonlocality strengths: purely local (left), weak nonlocality (middle), and representative nonlocality strength for InSb (right). (b) Electric field norm at the InSb/Si interface as a function of distance to the termination and nonlocality parameter β. (c) Dependence of the nonlocal backward-wave wave number in (b) versus nonlocality parameter β. The orange solid line shows the wave number as predicted by Eq. (14). (d) The maximum field enhancement follows the same inverse proportionality as the wave number. The orange line shows the maximum enhancement (in the absence of losses), while the purple line shows the results obtained with Eq. (12). Here, the field enhancement is measured against the field at the interface in the incoming surface wave.

is much larger than the forward one, implying large confinement and dissipation of the backward mode over short distances.

The peak field enhancement observed at the termination is a consequence of constructive interference between the forward and backward modes, as evidenced by the

beating pattern in Fig. 7(b). The enhancement at the interface is thus given by $|\mathbf{E}_f + \mathbf{E}_b|/|\mathbf{E}_f|$, where $\mathbf{E}_f$ and $\mathbf{E}_b$ are the forward and backward fields. We now estimate this factor based on a few simplifying factors. First, the field of a reciprocal plasmon in the electrostatic limit at an infinitesimal distance above the interface is given by $\mathbf{E} = 2e^{ikx}\sqrt{(\varepsilon_d + \varepsilon_m)P_0/\omega\varepsilon_0\varepsilon_d^2}\{-ik, k, 0\}$, where ε_d and ε_m are the dielectric and metal permittivities and P_0 is the power carried by the plasmon. For a fixed level of carried power, the electric field norm scales linearly with k (if frequency and permittivities are constant). Using this expression, we find for the enhancement

$$\frac{|\mathbf{E}_f + \mathbf{E}_b|}{|\mathbf{E}_f|} \approx \frac{|k_f e^{-ik_f x} + rk_{\mathrm{NL}}e^{ik_{\mathrm{NL}}x}|}{|k_f|}, \qquad (11)$$

where k_f is the forward wave number, k_{NL} is the backward nonlocal wave number, and r is the phase factor picked up by reflection at the termination. Assuming that the wave numbers are real and that the reflection phase is -1 (since the termination is a PEC), the first peak in enhancement is at $x = \pi/(k_f + k_{\mathrm{NL}})$. Considering losses, we thus find for the enhancement factor:

$$\frac{|\mathbf{E}_f + \mathbf{E}_b|}{|\mathbf{E}_f|} \approx \frac{|k_f - k_{\mathrm{NL}}e^{-\mathrm{Im}(k_{\mathrm{NL}})x}|}{|k_f|} \approx \frac{|k_{\mathrm{NL}}|}{|k_f|}e^{-\mathrm{Im}(k_{\mathrm{NL}})x}, \qquad (12)$$

as generally $k_{\mathrm{NL}} \gg k_f$ and the decay of the forward mode can safely be ignored. With exact knowledge of the wave numbers, this expression can be evaluated directly. In the following, however, we derive an approximate expression that enables evaluation based only on the material parameters.

First, we estimate the real part of k_{NL}. The backward wave number is expected to vary linearly with β, based on the linear scaling of the characteristic nonlocal length scale $\xi \sim \beta/\omega$. In the electrostatic limit ($k \gg \omega/c$), the dispersion equation for a reciprocal surface plasmon may be written as [75,76]

$$\omega(k) = \frac{\omega_p}{\sqrt{\varepsilon_\infty + \varepsilon_r}}\left[1 + \sqrt{\frac{\varepsilon_r(\varepsilon_\infty + \varepsilon_r)}{4\varepsilon_\infty}}\frac{\beta}{\omega_p}k\right] + \mathcal{O}(k^2). \qquad (13)$$

The correction to the dispersion due to nonlocal effects indeed scales (to first order) with β/ω_p, and this linear relationship can be verified by calculating the Fourier spectrum of the fields and extracting the backwards wave number, as plotted in Fig. 7(c). We observe that the nonlocal backward mode k_{NL} indeed scales inversely proportional to β. By rewriting Eq. (13) we obtain an expression for the backwards wave number in the reciprocal case. A straightforward correction to account for the magnetic bias is to

replace the plasma frequency with the backward asymptote in the nonreciprocal case, $\omega_{sp}^{(-)} = (\sqrt{4\omega_p^2 + \omega_c^2} - \omega_c)/2$ [10]. This yields as an approximation for the nonlocal backward wave number:

$$k_{\mathrm{NL}} = \frac{2}{\beta}\sqrt{\frac{\varepsilon_\infty}{\varepsilon_r}}[\omega - \omega_{sp}^{(-)}]. \qquad (14)$$

This simple approximation is shown in Fig. 7(c), and agrees well with the results obtained from the Fourier transform. Even better agreement may likely be obtained by considering the gyrotropy directly in deriving an electrostatic dispersion relationship.

Next, we consider losses in the backward mode. We use first-order perturbation theory [77],

$$k = k^{(0)} + i\omega\mathrm{Im}(\varepsilon_m)\frac{\int \mathbf{E} \cdot \mathbf{E}^* dl}{2\int \mathrm{Re}(\mathbf{E} \times \mathbf{H}^*) \cdot d\mathbf{l}}, \qquad (15)$$

where $k^{(0)}$ is the unperturbed propagation constant, and in this particular case we consider the perturbation to be $\Delta\varepsilon = \mathrm{Im}(\varepsilon_m)$. We can evaluate this expression analytically for a reciprocal plasmon, again, in which case we obtain

$$k_{\mathrm{NL}} = k_{\mathrm{NL}}^{(0)} - i\frac{\mathrm{Im}(\varepsilon_m)\varepsilon_r\kappa_d}{2\mathrm{Re}(\varepsilon_m)\kappa_m}\frac{\kappa_d^2 + \kappa_m^2}{\kappa_d\varepsilon_r + \kappa_m\mathrm{Re}(\varepsilon_m)}$$

$$\approx k_{\mathrm{NL}}^{(0)}\left[1 - i\frac{\mathrm{Im}(\varepsilon_m)}{\mathrm{Re}(\varepsilon_m)}\frac{\varepsilon_r}{\varepsilon_r + \mathrm{Re}(\varepsilon_m)}\right]. \qquad (16)$$

Here $\kappa_i^2 = k_{\mathrm{NL}}^2 - \varepsilon_i k_0^2$ are the transverse wave numbers in each material and $k_{\mathrm{NL}}^{(0)}$ is calculated using Eq. (14) assuming no losses.

Finally, the forward wave number can be accurately approximated by taking the reciprocal plasmon dispersion and adjusting the plasma frequency so that the plasmon asymptote occurs at the same frequency as in the nonreciprocal scenario, $\omega_{sp}^{(+)} = (\sqrt{4\omega_p^2 + \omega_c^2} + \omega_c)/2$ [10]. This yields for the forward dispersion:

$$k_f \approx \sqrt{\frac{\varepsilon_d\varepsilon_{m(+)}}{\varepsilon_d + \varepsilon_{m(+)}}}k_0, \qquad (17)$$

where $\varepsilon_{m(+)} = 1 - \omega_{p(+)}^2/\omega^2$ is the Drude dispersion with the plasma frequency replaced by an effective plasma frequency capturing the location of the upper asymptote:

$$\omega_{p(+)} = \sqrt{\omega_p^2 + \frac{\omega_c^2(\varepsilon_r + \varepsilon_\infty)}{\varepsilon_\infty}} + \sqrt{\frac{\varepsilon_r + \varepsilon_\infty}{\varepsilon_\infty}}\omega_c. \qquad (18)$$

While we make a number of approximations, in particular making simple corrections to account for the gyrotropy, the resulting expression for the field enhancement is still rather

accurate. This can be observed in Fig. 7(d), where we show the maximum field enhancement (relative to the field in the incoming surface plasmon), compared to the upper limit of enhancement $|k_{NL}|/|k_f|$ and the enhancement as predicted by Eqs. (12), (14), and (16). The agreement with the approximation is excellent up to very large nonlocal parameters, and as expected from Eqs. (12) and (14) we observe that $|\mathbf{E}| \propto |k_{NL}| \propto \beta^{-1}$.

The dependence of the field enhancement on β [69] observed in Figs. 7(b)–7(d) indicates that it is of considerable interest to engineer a plasmonic material with small β/ω_p. As noted previously, the plasma frequency $\omega_p = \sqrt{ne^2/\varepsilon_0 m_e}$, while β depends on the nature of the electron gas [50]:

$$\beta = \begin{cases} 3k_B T/m_e & \text{(nondegenerate)} \\ \sqrt{\dfrac{3}{5}\dfrac{\hbar^2}{m_e^2}(3\pi^2 n)^{2/3}} & \text{(degenerate)} \end{cases}, \quad (19)$$

which yields

$$\frac{\beta}{\omega_p} \propto \begin{cases} \dfrac{1}{(m_e n)^{1/2}} & \text{(nondegenerate)} \\ \dfrac{1}{m_e^{1/2} n^{1/6}} & \text{(degenerate)} \end{cases}. \quad (20)$$

In both cases, the ratio is inversely proportional to the effective electron mass and the doping density. Using a material with larger effective mass hence reduces the characteristic nonlocal length. On the other hand, the relative unidirectional frequency window that can be opened follows the same scaling: $\omega_c/\omega_p \propto 1/(m_e n)^{1/2}$. As a result, for fixed magnetic bias strength, we find that, as the field enhancement increases due to smaller β/ω_p, the unidirectional bandwidth is simultaneously reduced. Interestingly, the bandwidth-enhancement product, the figure of merit we introduce in this paper, is thus approximately conserved for nonreciprocal hotspots for fixed magnetic fields. For given magnetic field strengths, the maximum relative unidirectional gap that can be opened is $\omega_c/\omega_p = \varepsilon_d/\sqrt{2(\varepsilon_\infty + \varepsilon_d)(2\varepsilon_\infty + \varepsilon_d)}$ [10], indicating that it is always advantageous to reduce nonlocality.

A larger effective mass can generally be found in semiconductors with larger band gaps, such as germanium ($m_e = 0.12 m_0$) and aluminum nitride ($m_e = 0.4 m_0$). For example, using AlN instead of InSb results in a characteristic length β/ω_p approximately 6 times smaller for the same electron density. Due to the larger effective mass, however, a 100-fold increase in doping density can likely be achieved before the electron gas becomes degenerate. These considerations imply that β/ω_p may be roughly 60 times smaller, which, according to Figs. 7(b) and 7(d), indicates that significant field-enhancement factors are achievable.

A potential downside of using wider band-gap semiconductors is that their mobility also tends to be significantly lower. In fact, because of its low effective mass, InSb also has one of the highest electron mobilities among semiconductors, leading to a relatively low scattering rate γ. The experimentally observed mobility in AlN is roughly 250 times lower, resulting in a scattering rate almost equal to the plasma frequency for moderate doping levels (and higher doping levels would further increase impurity scattering). It would therefore be interesting to explore quantum-engineered materials with *large* effective masses yet high intrinsic carrier concentrations, so that impurity scattering can be minimized. Using semiconductor superlattices [78], for example, it has been have shown that infinite effective masses are achievable by taking a metamaterial-inspired design approach [79,80]. Similarly, it has been demonstrated that the effective mass of electrons in graphene can be modified through periodic potentials [81,82]. These represent promising avenues to pursue shorter nonlocality lengths, in addition to using, e.g., actual gas plasmas (where the effective mass is the one of a free electron and losses are very low) or pursuing "hole plasmonics," because holes have large effective masses (but losses may be significant).

VIII. SURFACE ROUGHNESS

Unidirectional waveguides are particularly interesting for nanophotonic applications because of their unique features in protecting optical transport against disorder. One type of disorder that cannot be fully eliminated is surface roughness, which, for example, is the limiting factor in photonic crystal slow light waveguides [83,84]. In truly unidirectional waveguides, backscattering losses can simply not occur due to the absence of the backwards mode. As we discuss in the previous section, however, in the unidirectional waveguide discussed so far, a backwards mode appears due to the nonlocal nature of the permittivity. Just as some degree of surface roughness can ultimately not be prevented, all physical systems will ultimately also be nonlocal. In the next section, we discuss topologically protected unidirectional waveguides that maintain unidirectionality even in the presence of nonlocality. First, however, we investigate how surface roughness actually affects the performance of the nonlocal unidirectional waveguides discussed in the previous section.

To start, we consider the effect of surface roughness on transmission for a local reciprocal system and the nonlocal unidirectional waveguide. We numerically calculate transmission past a finite length of exaggerated surface roughness (rms of 38 nm, see Appendix) on the interface between InSb and Si, shown in Fig. 8(a). In order to assess the effect of surface roughness, the forward wave number in the reciprocal and nonreciprocal systems are identical, and the loss rate is reduced by a factor of four. For
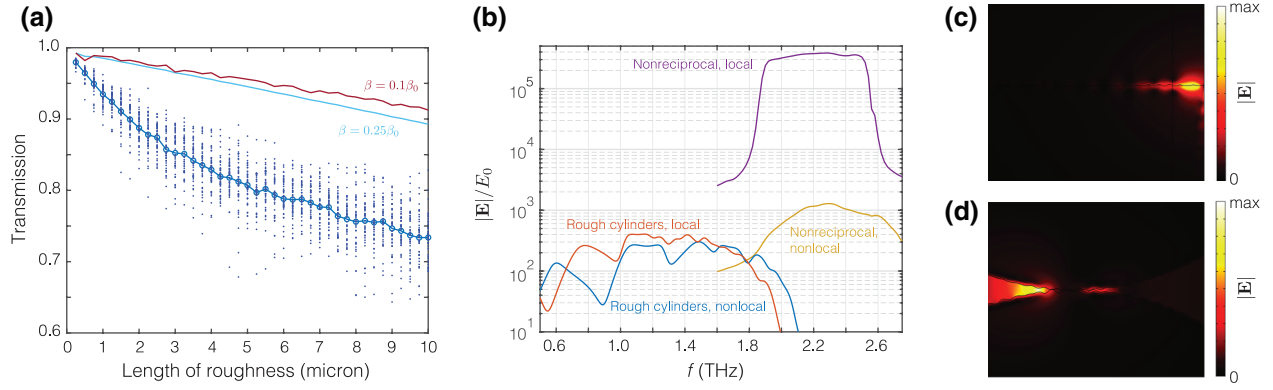
FIG. 8.   (a) Transmission as a function of length of a section of surface roughness (rms = 32 nm). The reciprocal scenario (2.05 THz) is much more susceptible to roughness than the nonlocal, nonreciprocal scenarios are (2.15 THz). In this panel the loss rate is reduced by a factor of 4 to make roughness effects more visible. (b) Maximum field enhancement in the touching cylinders and terminated waveguide when surface roughness is included with (rms = 4 nm, loss rate also reduced by a factor 4). The touching cylinders (red and blue) are significantly affected by the surface roughness, compared to Fig. 4, while nonreciprocity (purple and yellow) limits the effects of surface roughness, and the main reduction in field enhancement is caused by nonlocality itself. (c) In the rough touching cylinders, the maximum enhancement no longer occurs exactly at the apex, but between two rough extrusions where the metal cylinders are in very close proximity. (d) The field norm near the termination in the rough scenario, which is very similar to the enhancement observed in Fig. 7.

the reciprocal plasmonic waveguide, we observe a strong dependence on the exact shape of the roughness: Fig. 8(a) shows the transmission of many simulations for different random roughness and roughness lengths (shown by blue dots), together with the averaged transmission (blue line). The transmission strongly depends on the roughness due to the formation of standing waves. In contrast, for the nonlocal unidirectional scenarios we do not observe variation with the exact shape of the roughness, and what is more, the effect of surface roughness is much less significant. While in the reciprocal scenario there is considerable forward and backward scattering, in the unidirectional, nonlocal scenario the backward waves are largely absorbed before they can contribute to standing waves. These results show that, while a backward channel appears when nonlocality is considered [70], there are still significant benefits to these nonreciprocal waveguides.

Next, to place the resilience of the nonreciprocal waveguide to disorder into context, in Fig. 8(b) we again compare the maximum field enhancement in the terminated waveguide and touching cylinder geometries. In this case, however, we also include surface roughness (rms 4 nm) and nonlocality ($\beta = 0.1\beta_{InSb}$). The field enhancement and continuous bandwidth of the touching cylinders are both reduced with respect to the smooth scenario (peak enhancement of 3×10^3). The lower performance is a consequence of the extremely high field strengths near the apex, which make the structure very susceptible to even small perturbations. On the other hand, the local unidirectional waveguide barely sacrifices performance relative to the smooth surface (peak enhancement of 3×10^5)—since

backscattering is not possible. Including nonlocality, however, results in a drop in the field enhancement in line with what is observed in Fig. 7, and the surface roughness appears to play a minimal role. This is in agreement with Fig. 8(a): as surface roughness only results in some additional attenuation in the nonreciprocal scenario, rather than the emergence of strong back-and-forth scattering and the formation of standing waves as in the reciprocal scenario, the impact of roughness on the field enhancement can also be expected to be minimal.

The maximum field enhancement in the touching cylinders occurs between two extruding parts of surface roughness, where the two metal spheres approach closely, as can be observed in Fig. 8(c). This is in contrast to the smooth cylinders, where the peak enhancement occurs very close to the apex. For the nonreciprocal terminated waveguide, however, the behavior is extremely similar to that of the smooth terminated waveguide: in Fig. 8(d) we observe again the interference between the forward and backward waves. This further exemplifies the robustness of the nonreciprocal waveguides to surface roughness, even in the presence of nonlocality.

IX. HOTSPOTS IN PHOTONIC TOPOLOGICAL INSULATORS

In close analogy with the unidirectional polaritonic waveguides discussed so far, unidirectional edge states can arise at the interface between media with different band-structure topologies [8,14]. Photonic topological insulators have been typically discussed in the context of periodic
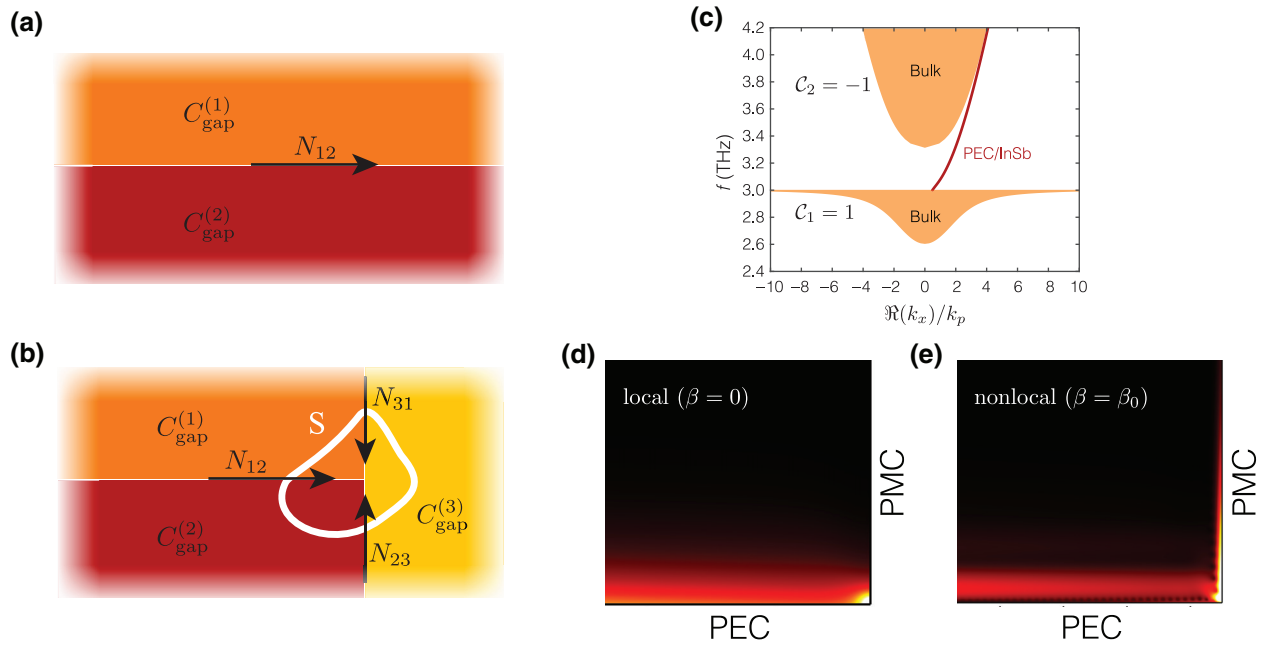
FIG. 9.   (a) The number of topologically protected edge states N_{12} at an interface between two media with gap Chern numbers $C_{\text{gap}}^{(i)}$ is given by the difference of their gap Chern numbers. (b) Modal dispersion of the PEC and magnetized plasma interface, supporting a topologically protected edge state between the two bulk bands. (c) A termination, such as the nonreciprocal hotspot discussed in this work, occurs at the interface of (at least) three different materials. Equation (17) shows that, independent of the number of materials comprising a junction, the number of edge states crossing a boundary S must add up to 0 (where the sign of N_{ij} determines the direction into or out of the domain). This means that true topologically protected terminations cannot exist. (d) As a result, a surface wave at the PEC and magnetized plasma wave terminated by a PMC forms a hotspot, analogous to the hotspot discussed earlier in this work. (e) When including nonlocality, the outgoing mode traveling along the PMC becomes apparent, validating Eq. (17).

photonic crystals, in which nontrivial band structures are obtained by breaking time-reversal symmetry. The band-structure topology is characterized by a topological invariant, the Chern number c_n, which is calculated as the integrated Berry flux over the entire Brillouin zone [85]. This integer is robust against perturbations, and a topological phase transition is required to modify the Chern number: hence, at the interface between two media with different topological invariant the gap between them is closed by an edge state traversing the entire gap [86]. The interest in photonic topological insulators arises because edge states are impervious to obstructions [7,8], enabling robust transport of information or delay lines protected against disorder [12,87].

The number of supported edge states at an interface between two media, and their direction of propagation, is directly related to the difference of the gap topological invariant of the two materials through the so-called bulk-edge correspondence [88]

$$N_{12} = c_{\text{gap}}^{(1)} - c_{\text{gap}}^{(2)}, \qquad (21)$$

as shown in Fig. 9(a). Here, $c_{\text{gap}}^{(1)}$ is the gap Chern number associated with the band gap of medium 1, defined as the sum of all band Chern numbers below the frequency of

operation (including negative frequencies):

$$c_{\text{gap}} = \sum c_n. \qquad (22)$$

While photonic topological insulators have been most commonly implemented in photonic crystals, for which it is easier to define topological invariants, it is also possible to ascribe Chern numbers to continuous media, such as the magnetically biased plasma discussed so far [89], as shown in the band structure in Fig. 9(b). To be able to perform the integration over the band structure, nonlocality must be explicitly included, which introduces a spatial cutoff and allows the integration. The topological invariants are calculated as $c_1 = 1$ and $c_2 = -1$, i.e., the gap between the first and second band has a nontrivial topological invariant $c_{\text{gap}} = 1$, resulting in a unidirectional edge state when interfaced with a topologically trivial, opaque medium, seen in Fig. 9(b) (red line).

The unidirectional waveguide considered in the previous sections is operated below the first bulk band, where $c_{\text{gap}} = 0$ and no topologically protected edge state is expected. Indeed, as we discuss, when nonlocality is explicitly included the unidirectional nature of this waveguide vanishes, limiting the overall field enhancement. On the other hand, the topologically protected edge state

shown in Fig. 9(b), emerging at higher frequencies, is robust against nonlocality [45]. It is therefore natural to wonder whether these topologically protected edge states may provide a viable pathway to nonreciprocal hotspots arising at a termination, without the detrimental effects of nonlocality.

Here, we provide a basic argument that such nonreciprocal edge modes may be of limited appeal for this application. As schematically shown in Fig. 9(c), it is not possible to terminate the unidirectional waveguide with just two materials. Creating a nonreciprocal termination requires at least a third material, but can in principle involve as many materials as necessary. Figure 9(c) shows an example of a termination consisting of three materials, where the junction is enclosed by the surface S. A nonreciprocal hotspot fed by a unidirectional mode traveling along the interface between materials 1 and 2 would require $N_{12} = 1$, $N_{23} = 0$, and $N_{31} = 0$, so that energy accumulates at the junction. In this case, the sum of all edge states propagating into S is $\sum N_{ij} = 1$. However, starting from Eq. (21), with some rearranging we can readily show that

$$\sum N_{ij} = \sum [c_{\text{gap}}^{(i)} - c_{\text{gap}}^{(j)}] = \sum [c_{\text{gap}}^{(i)} - c_{\text{gap}}^{(i)}] = 0. \quad (23)$$

This result implies that, for topologically protected edge states, it is impossible to create a junction between multiple materials that has more edge states propagating into the surface S surrounding the junction, than propagating out of that surface. This identity, consistent with the second Kirchhoff law in electrical circuits, forbids accumulation of energy driven by topological edge states. Equation (23) applies to any number of interfaces between materials.

To explore the implications of Eq. (23) we now consider the implementation of a hotspot using the topologically protected edge state in Fig. 9(b), as studied in Refs. [22,45]. The system consists of a magnetically biased plasmonic material, as in the previous sections, but interfaced directly with a PEC wall. The termination consists of a perfect magnetic conducting (PMC) wall. This specific geometry has been studied in the context of nonreciprocal hotspots by Ishimaru in 1962 [16], who showed that the hotspot dissipates all incoming power from the unidirectional waveguide even in the limit of zero losses, resolving the thermodynamic paradox that appears to emerge in lossless unidirectional waveguides [21,90]. This configuration regained interest when it was shown that, with suitable spatial dispersion, the bulk bands of the plasma have topologically nontrivial features [89]. As such, the unidirectional edge states that arise in this system also persist in the presence of nonlocality [45].

The termination with a PMC in the local case is shown in Fig. 9(d), where a hotspot similar to Fig. 3 is clearly visible. There is also no edge state along the PMC wall, in agreement with Ishimaru and others [16,45]. However, this finding simultaneously contradicts Eq. (23), which

requires, for any topologically protected edge state feeding a node, an equal number of edge states leaving the same node. The contradiction between Eq. (23) and Fig. 9(d) is resolved when we consider nonlocality, which is required for the same definition of a topological band [89]. Including nonlocality indeed results in a clearly visible edge state along the PMC boundary, propagating away from the junction, as shown in Fig. 9(e). This edge state is still highly confined and it dissipates quickly for realistic levels of loss, as shown here. In the limit of $\beta \to 0$ the wave number approaches infinity, resulting in an infinitely confined mode that cannot be observed [91].

Figure 9(e) clearly demonstrates that, indeed, an equal number of edge states enter and exit a small surface enclosing the junction between the PEC, PMC and magnetized plasma. However, this does not imply that topologically protected edge states cannot lead to large field enhancements. First of all, we simultaneously observe a significant field enhancement at the termination, which originates from the high confinement of the outgoing edge state, similar to the backward mode considered in the previous section. These results imply that unidirectional topological and nonreciprocal waveguides appear to always support outgoing modes driven by nonlocality. For sufficiently small nonlocality and losses, both these platforms still ensure large field confinement over large bandwidths.

Finally, an alternative approach to implement electromagnetic hotspots may consist in using *reciprocal* topological photonic insulators. These systems have zero Chern number, indicating that they cannot support truly protected unidirectional edge states. However, there are other degrees of freedom, such as the photonic spin [92–95] and valley [96,97], that can be ascribed topological invariants, and allow for quasi-unidirectional properties as long as the crystal symmetry is maintained. While these systems will always support a time-reversed backward edge channel, with opposite spin or valley, suitably designed terminations may poorly couple with these outgoing fields, so that a significant amount of energy can be stored at the junction. As an example, hotspots have been recently shown at the interface between two materials with opposite valley-Chern number and a PEC termination [98], opening interesting opportunities for the applications mentioned in this work, provided that suitable termination geometries are considered.

X. CONCLUSIONS

In this work, we discuss the properties and potential applications of electromagnetic hotspots at the termination of nonreciprocal and topological waveguides for nanophotonic applications. Nonreciprocal hotspots exhibit extremely large field strengths in ultraconfined volumes over very large bandwidths, overcoming the fundamental trade-offs between bandwidth, field confinement, footprint,

and robustness to disorder that commonly impact various classical and quantum photonic applications. We show how the unusual features of nonreciprocal hotspots support exhibit extremely large and broadband LDOS enhancements and harmonic generation efficiencies. We also discuss the general impact of loss and nonlocality on these phenomena, which fundamentally limit the achievable field confinement. In this context, we propose a path towards optimal material engineering to maximize these responses. Finally, we outline how, in topologically trivial nonreciprocal waveguides, nonlocality induces a backward mode with large wave number and, in the case of topological interface modes, nonlocality requires trickling of the energy in other outgoing channels. Interestingly, therefore, nonlocality appears to generally forbid field singularities in all known classes of nonreciprocal waveguides, yet for realistic levels of nonlocality in intrinsic semiconductors and quantum engineered materials we find that significant field confinement over broad bandwidths can be expected at the hotspots, and even reciprocal topological systems with properly terminated interfaces may support similar responses. Our findings open exciting opportunities in classical and quantum nanophotonic systems, spanning from single-photon generation and confined sources to largely enhanced nonlinear responses over broad bandwidths, beyond the limits of conventional plasmonic approaches. These results may also be translated into wave physics domains beyond optics, such as acoustics, particularly considering topological phenomena for which plasmonics is not required.

ACKNOWLEDGMENTS

APPENDIX: METHODS

All numerical results presented here are obtained with COMSOL Multiphysics v5.5. To achieve convergence, the mesh sizes employed near the hotspot have to be extremely small to capture the singularity, on the order of 10^{-10} m or under one millionth of the free-space wavelength. The nonlinearity in Fig. 6 is implemented by first calculating the fields at the fundamental frequency, and then taking Eq. (8) as an external current density source in a separate simulation at the second harmonic. The nonlocal results in Figs. 7 and 8 are calculated by adding a weak form partial-differential equation, Eq. (9), for the current densities. The solution of this PDE is then fed back into the local simulation as an external current density. To create a random rough surface, a parametric curve is generated from a sum of sines with random amplitudes, drawn from a Gaussian distribution, and uniform random phases.

[1] J. A. Schuller, E. S. Barnard, W. Cai, Y. C. Jun, J. S. White, and M. L. Brongersma, Plasmonics for extreme light concentration and manipulation, Nat. Mater. **9**, 193 (2010).

[2] R. Ameling, L. Langguth, M. Hentschel, M. Mesch, P. V. Braun, and H. Giessen, Cavity-enhanced localized plasmon resonance sensing, Appl. Phys. Lett. **97**, 1 (2010).

[3] A. Kinkhabwala, Z. Yu, S. Fan, Y. Avlasevich, K. Müllen, and W. E. Moerner, Large single-molecule fluorescence enhancements produced by a bowtie nanoantenna, Nat. Photonics **3**, 654 (2009).

[4] G. M. Akselrod, C. Argyropoulos, T. B. Hoang, C. Ciracì, C. Fang, J. Huang, D. R. Smith, and M. H. Mikkelsen, Probing the mechanisms of large Purcell enhancement in plasmonic nanoantennas, Nat. Photonics **8**, 835 (2014).

[5] R. Chikkaraddy, B. de Nijs, F. Benz, S. J. Barrow, O. A. Scherman, E. Rosta, A. Demetriadou, P. Fox, O. Hess, and J. J. Baumberg, Single-molecule strong coupling at room temperature in plasmonic nanocavities, Nature **535**, 127 (2016).

[6] Z. Yu, G. Veronis, Z. Wang, and S. Fan, One-Way Electromagnetic Waveguide Formed at the Interface Between a Plasmonic Metal Under a Static Magnetic Field and a Photonic Crystal, Phys. Rev. Lett. **100**, 023902 (2008).

[7] Z. Wang, Y. D. Chong, J. D. Joannopoulos, and M. Soljačić, Reflection-Free One-Way Edge Modes in a Gyromagnetic Photonic Crystal, Phys. Rev. Lett. **100**, 013905 (2008).

[8] Z. Wang, Y. Chong, J. D. Joannopoulos, and M. Soljačić, Observation of unidirectional backscattering-immune topological electromagnetic states, Nature **461**, 772 (2009).

[9] J. Guglielmon and M. C. Rechtsman, Broadband Topological Slow Light Through Higher Momentum-Space Winding, Phys. Rev. Lett. **122**, 153904 (2019).

[10] L. Shen, Y. You, Z. Wang, and X. Deng, Backscattering-immune one-way surface magnetoplasmons at terahertz frequencies, Opt. Express **23**, 950 (2015).

[11] Y. Hadad and B. Z. Steinberg, One way optical waveguides for matched non-reciprocal nanoantennas with dynamic beam scanning functionality, Opt. Express **21**, A77 (2013).

[12] S. A. Mann, D. L. Sounas, and A. Alù, Broadband delay lines and nonreciprocal resonances in unidirectional waveguides, Phys. Rev. B **100**, 020303 (2019).

[13] O. Luukkonen, U. K. Chettiar, and N. Engheta, One-way waveguides connected to one-way loads, IEEE Antennas Wirel. Propag. Lett. **11**, 1398 (2012).

[14] F. D. M. Haldane and S. Raghu, Possible Realization of Directional Optical Waveguides in Photonic Crystals with Broken Time-Reversal Symmetry, Phys. Rev. Lett. **100**, 013904 (2008).

[15] T. Ozawa, H. M. Price, A. Amo, N. Goldman, M. Hafezi, L. Lu, M. C. Rechtsman, D. Schuster, J. Simon, O. Zilberberg, and I. Carusotto, Topological photonics, Rev. Mod. Phys. **91**, 015006 (2019).

[16] A. Ishimaru, Unidirectional Waves in Anisotropic Media and the Resolution of the Thermodynamic Paradox, Air Force Technical Rep. No. 69 (1962).

[17] G. Barzilai and G. Gerosa, Rectangular waveguides loaded with magnetised ferrite, and the so-called thermodynamic paradox, Proc. Inst. Electr. Eng. **113**, 285 (1966).

[18] U. K. Chettiar, A. R. Davoyan, and N. Engheta, Hotspots from nonreciprocal surface waves, Opt. Lett. **39**, 1760 (2014).

[19] L. Shen, X. Zheng, and X. Deng, Stopping terahertz radiation without backscattering over a broad band, Opt. Express **23**, 11790 (2015).

[20] M. Marvasti and B. Rejaei, Formation of hotspots in partially filled ferrite-loaded rectangular waveguides, J. Appl. Phys. **122**, 233901 (2017).

[21] S. A. Mann, D. L. Sounas, and A. Alù, Nonreciprocal cavities and the time–bandwidth limit, Optica **6**, 104 (2019).

[22] D. E. Fernandes and M. G. Silveirinha, Topological Origin of Electromagnetic Energy Sinks, Phys. Rev. Appl. **12**, 014021 (2019).

[23] E. M. Purcell, Spontaneous emission probabilities at radio frequencies, Phys. Rev **69**, 681 (1946).

[24] K. G. Cognée, W. Yan, F. La China, D. Balestri, F. Intonti, M. Gurioli, A. F. Koenderink, and P. Lalanne, Mapping complex mode volumes with cavity perturbation theory, Optica **6**, 269 (2019).

[25] A. F. Koenderink, On the use of Purcell factors for plasmon antennas, Opt. Lett. **35**, 4208 (2010).

[26] A. F. Koenderink, Single-photon nanoantennas, ACS Photonics **4**, 710 (2017).

[27] H. Fischer and O. J. F. Martin, Engineering the optical response of plasmonic nanoantennas, Opt. Express **16**, 9144 (2008).

[28] S. Dodson, M. Haggui, R. Bachelot, J. Plain, S. Li, and Q. Xiong, Optimizing electromagnetic hotspots in plasmonic bowtie nanoantennae, J. Phys. Chem. Lett. **4**, 496 (2013).

[29] S. Kim, J. Jin, Y.-J. Kim, I.-Y. Park, Y. Kim, and S.-W. Kim, High-harmonic generation by resonant plasmon field enhancement, Nature **453**, 757 (2008).

[30] J. N. Farahani, D. W. Pohl, H. J. Eisler, and B. Hecht, Single Quantum Dot Coupled to a Scanning Optical Antenna: A Tunable Superemitter, Phys. Rev. Lett. **95**, 1 (2005).

[31] M. I. Stockman, Nanofocusing of Optical Energy in Tapered Plasmonic Waveguides, Phys. Rev. Lett. **93**, 137404 (2004).

[32] D. F. P. Pile and D. K. Gramotnev, Adiabatic and nonadiabatic nanofocusing of plasmons by tapered gap plasmon waveguides, Appl. Phys. Lett. **89**, 2004 (2006).

[33] E. Verhagen, A. Polman, and L. K. Kuipers, Nanofocusing in laterally tapered plasmonic waveguides, Opt. Express **16**, 45 (2008).

[34] H. Choo, M.-K. Kim, M. Staffaroni, T. J. Seok, J. Bokor, S. Cabrini, P. J. Schuck, M. C. Wu, and E. Yablonovitch, Nanofocusing in a metal–insulator–metal gap plasmon waveguide with a three-dimensional linear taper, Nat. Photonics **6**, 838 (2012).

[35] D. K. Gramotnev and S. I. Bozhevolnyi, Nanofocusing of electromagnetic radiation, Nat. Photonics **8**, 13 (2014).

[36] J. A. Dionne, L. A. Sweatlock, H. A. Atwater, and A. Polman, Plasmon slot waveguides: Towards chip-scale propagation with subwavelength-scale localization, Phys. Rev. B **73**, 035407 (2006).

[37] ŞE Kocabaş, G. Veronis, D. A. B. Miller, and S. Fan, Modal analysis and coupling in metal-insulator-metal waveguides, Phys. Rev. B **79**, 035120 (2009).

[38] J. G. Van Bladel, *Singular Electromagnetic Fields and Sources* (Oxford University Press, Oxford, UK, 1991).

[39] M. G. Silveirinha and N. Engheta, Theory of supercoupling, squeezing wave energy, and field confinement in narrow channels and tight bends using -near-zero metamaterials, Phys. Rev. B **76**, 245109 (2007).

[40] N. M. Estakhri and A. Alù, Physics of unbounded, broadband absorption/gain efficiency in plasmonic nanoparticles,", Phys. Rev. B **87**, 205418 (2013).

[41] J. B. Pendry, A. Aubry, D. R. Smith, and S. A. Maier, Transformation optics and subwavelength control of light, Science **337**, 549 (2012).

[42] J. B. Pendry, P. A. Huidobro, Y. Luo, and E. Galiffi, Compacted dimensions and singular plasmonic surfaces, Science **358**, 915 (2017).

[43] D. Y. Lei, A. Aubry, S. A. Maier, and J. B. Pendry, Broadband nano-focusing of light using kissing nanowires, New J. Phys. **12**, 093030 (2010).

[44] A. Aubry, D. Y. Lei, A. I. Fernández-Domínguez, Y. Sonnefraud, S. A. Maier, and J. B. Pendry, Plasmonic light-harvesting devices over the whole visible spectrum, Nano Lett. **10**, 2574 (2010).

[45] S. A. Hassani Gangaraj and F. Monticone, Do truly unidirectional surface plasmon-polaritons exist?, Optica **6**, 1158 (2019).

[46] J. A. Bittencourt, *Fundamentals of Plasma Physics*, 3rd ed. (Springer-Verlag, New York, 2010).

[47] O. V. Kotov and Y. E. Lozovik, Giant tunable nonreciprocity of light in Weyl semimetals, Phys. Rev. B **98**, 195446 (2018).

[48] B. Zhao, C. Guo, C. A. C. Garcia, P. Narang, and S. Fan, Axion-field-enabled nonreciprocal thermal radiation in Weyl semimetals, Nano Lett. **20**, 1923 (2020).

[49] J. J. Brion, R. F. Wallis, A. Hartstein, and E. Burstein, Theory of Surface Magnetoplasmons in Semiconductors, Phys. Rev. Lett. **28**, 1455 (1972).

[50] J. R. Maack, N. A. Mortensen, and M. Wubs, Size-dependent nonlocal effects in plasmonic semiconductor particles, Europhysics Lett. **119**, 17003 (2017).

[51] B. van der Pol, On the wave-lengths and radiation of loaded antennae, Proc. Phys. Soc. London **29**, 269 (1917).

[52] K. H. Drexhage, Influence of a dielectric interface on fluoresence decay time, J. Lumin. **2**, 693 (1970).

[53] E. Johlin, J. Solari, S. A. Mann, J. Wang, T. S. Shimizu, and E. C. Garnett, Super-resolution imaging of light–matter interactions near single semiconductor nanowires, Nat. Commun. **7**, 13950 (2016).

[54] L. Langguth, R. Fleury, A. Alù, and A. F. Koenderink, Drexhage's Experiment for Sound, Phys. Rev. Lett. **116**, 1 (2016).

[55] R. Sprik, B. A. van Tiggelen, and A. Lagendijk, Optical emission in periodic dielectrics, Europhys. Lett. **35**, 265 (1996).

[56] B. Lounis and M. Orrit, Single-photon sources, Reports Prog. Phys. **68**, 1129 (2005).

[57] P. Lodahl, S. Mahmoodian, and S. Stobbe, Interfacing single photons and single quantum dots with photonic nanostructures, Rev. Mod. Phys. **87**, 347 (2015).

[58] V. A. Dmitriev, Space-Time reversal symmetry properties of electromagnetic Green's tensors for complex and bianisotropic media, Prog. Electromagn. Res. **48**, 145 (2004).

[59] V. Asadchy, M. S. Mirmoosa, A. Díaz-Rubio, S. Fan, and S. A. Tretyakov, Tutorial on Electromagnetic Nonreciprocity and Its Origins, arXiv:2001.04848 (2020).

[60] L. D. Lifshitz and E. M. L. Landau, Electrodynamics of continuous media, Am. J. Phys. **29**, 647 (1961).

[61] C. Caloz, A. Alù, S. Tretyakov, D. Sounas, K. Achouri, and Z.-L. Deck-Léger, Electromagnetic Nonreciprocity, Phys. Rev. Appl. **10**, 047001 (2018).

[62] H. B. G. Casimir, On Onsager's principle of microscopic reversibility, Rev. Mod. Phys. **17**, 343 (1945).

[63] N. Rivera, I. Kaminer, B. Zhen, J. D. Joannopoulos, and M. Soljačić, Shrinking light to allow forbidden transitions on the atomic scale, Science **353**, 263 (2016).

[64] A. González-Tudela, P. A. Huidobro, L. Martín-Moreno, C. Tejedor, and F. J. García-Vidal, Theory of Strong Coupling Between Quantum Emitters and Propagating Surface Plasmons, Phys. Rev. Lett. **110**, 126801 (2013).

[65] P. Törmä and W. L. Barnes, Strong coupling between surface plasmon polaritons and emitters: A review, Rep, Prog. Phys. **78**, 013901 (2015).

[66] J. Lee, M. Tymchenko, C. Argyropoulos, P.-Y. Chen, F. Lu, F. Demmerle, G. Boehm, M.-C. Amann, A. Alù, and M. A. Belkin, Giant nonlinear response from plasmonic metasurfaces coupled to intersubband transitions, Nature **511**, 65 (2014).

[67] J. Lee, N. Nookala, J. S. Gomez-Diaz, M. Tymchenko, F. Demmerle, G. Boehm, M. Amann, A. Alù, and M. A. Belkin, Ultrathin second-harmonic metasurfaces with record-high nonlinear optical response, Adv. Opt. Mater. **4**, 664 (2016).

[68] S. A. Hassani Gangaraj, B. Jin, C. Argyropoulos, and F. Monticone, Broadband Field Enhancement and Giant Nonlinear Effects in Terminated Unidirectional Plasmonic Waveguides, Phys. Rev. Appl. **14**, 054061 (2020).

[69] C. Ciracì, R. T. Hill, J. J. Mock, Y. Urzhumov, A. I. Fernández-Domínguez, S. A. Maier, J. B. Pendry, A. Chilkoti, and D. R. Smith, Probing the ultimate limits of plasmonic enhancement, Science **337**, 1072 (2012).

[70] S. Buddhiraju, Y. Shi, A. Song, C. Wojcik, M. Minkov, I. A. D. Williamson, A. Dutt, and S. Fan, Absence of unidirectionally propagating surface plasmon-polaritons at nonreciprocal metal-dielectric interfaces, Nat. Commun. **11**, 674 (2020).

[71] F. Bloch, Bremsvermögen von Atomen mit mehreren Elektronen, Zeitschrift für Phys. **81**, 363 (1933).

[72] S. Raza, S. I. Bozhevolnyi, M. Wubs, and N. Asger Mortensen, Nonlocal optical response in metallic nanostructures, J. Phys. Condens. Matter **27**, 183204 (2015).

[73] N. A. Mortensen, Nonlocal formalism for nanoplasmonics: Phenomenological and semi-classical considerations, Photonics Nanostructures - Fundam. Appl. **11**, 303 (2013).

[74] P. Lalanne, S. Coudert, G. Duchateau, S. Dilhaire, and K. Vynck, Structural slow waves: Parallels between photonic crystals and plasmonic waveguides, ACS Photonics **6**, 4 (2019).

[75] A. D. Boardman, *Electromagnetic Surface Modes* (John Wiley & Sons, Ltd, Chichester, 1982).

[76] S. Raza, T. Christensen, M. Wubs, S. I. Bozhevolnyi, and N. A. Mortensen, Nonlocal response in thin-film waveguides: Loss versus nonlocality and breaking of complementarity, Phys. Rev. B **88**, 115401 (2013).

[77] R. F. Harrington, *Time-Harmonic Electromagnetic Fields*, (Wiley-IEEE, New York, 2001).

[78] L. Esaki and R. Tsu, Superlattice and negative differential conductivity in semiconductors, IBM J. Res. Dev. **14**, 61 (1970).

[79] M. G. Silveirinha and N. Engheta, Transformation electronics: Tailoring the effective mass of electrons, Phys. Rev. B **86**, 161104 (2012).

[80] M. G. Silveirinha and N. Engheta, Metamaterial-inspired model for electron waves in bulk semiconductors, Phys. Rev. B **86**, 245302 (2012).

[81] C.-H. Park, L. Yang, Y.-W. Son, M. L. Cohen, and S. G. Louie, Anisotropic behaviours of massless Dirac fermions in graphene under periodic potentials, Nat. Phys. **4**, 213 (2008).

[82] M. G. Silveirinha and N. Engheta, Effective medium approach to electron waves: Graphene superlattices, Phys. Rev. B **85**, 195413 (2012).

[83] S. Hughes, L. Ramunno, J. F. Young, and J. E. Sipe, Extrinsic Optical Scattering Loss in Photonic Crystal Waveguides: Role of Fabrication Disorder and Photon Group Velocity, Phys. Rev. Lett. **94**, 033903 (2005).

[84] E. Kuramochi, M. Hughes, A. Shinya, T. Watanabe, and L. Ramunno, Disorder-induced scattering loss of line-defect waveguides in photonic crystal slabs, Phys. Rev. B – Condens. Matter Mater. Phys. **72**, 161318 (2005).

[85] M. Blanco de Paz, C. Devescovi, G. Giedke, J. J. Saenz, M. G. Vergniory, B. Bradlyn, D. Bercioux, and A. García-Etxarri, Tutorial: Computing topological invariants in 2D photonic crystals, Adv. Quantum Technol. **3**, 1900117 (2020).

[86] L. Lu, J. D. Joannopoulos, and M. Soljačić, Topological photonics, Nat. Photonics **8**, 821 (2014).

[87] M. Hafezi, E. A. Demler, M. D. Lukin, and J. M. Taylor, Robust optical delay lines with topological protection, Nat. Phys. **7**, 907 (2011).

[88] M. G. Silveirinha, Proof of the bulk-edge correspondence through a link between topological photonics and fluctuation-electrodynamics, Phys. Rev. X **9**, 011037 (2019).

[89] M. G. Silveirinha, Chern invariants for continuous media, Phys. Rev. B **92**, 125153 (2015).

[90] B. Lax and K. J. Button, New ferrite mode configurations and their applications, J. Appl. Phys. **26**, 1186 (1955).

[91] S. A. Hassani Gangaraj and F. Monticone, Physical Violations of the Bulk-Edge Correspondence in Topological Electromagnetics, Phys. Rev. Lett. **124**, 153901 (2020).

[92] L.-H. Wu and X. Hu, Scheme for Achieving a Topological Photonic Crystal by Using Dielectric Material, Phys. Rev. Lett. **114**, 223901 (2015).

[93] S. Barik, H. Miyake, W. DeGottardi, E. Waks, and M. Hafezi, Two-dimensionally confined topological edge states in photonic crystals, New J. Phys. **18**, 113013 (2016).

[94] S. Barik, A. Karasahin, C. Flower, T. Cai, H. Miyake, W. DeGottardi, M. Hafezi, and E. Waks, A topological quantum optics interface, Science **359**, 666 (2018).

[95] N. Parappurath, F. Alpeggiani, L. Kuipers, and E. Verhagen, Direct observation of topological edge states in silicon photonic crystals: Spin, dispersion, and chiral routing, Sci. Adv. **6**, eaaw4137 (2020).

[96] T. Ma and G. Shvets, All-Si valley-Hall photonic topological insulator, New J. Phys. **18**, 025012 (2016).

[97] F. Gao, H. Xue, Z. Yang, K. Lai, Y. Yu, X. Lin, Y. Chong, G. Shvets, and B. Zhang, Topologically protected refraction of robust kink states in valley photonic crystals, Nat. Phys. **14**, 140 (2018).

[98] Y. Li, Y. Yu, F. Liu, B. Zhang, and G. Shvets, A Topology-Controlled Photonic Cavity Based on the Near-Conservation of the Valley Degree of Freedom, Phys. Rev. Lett. **125**, 213902 (2020).